ELSEVIER

Ultramicroscopy 59 (1995) 71–79

ultramicroscopy

Cryo-electron energy loss spectroscopy: observations on vitrified hydrated specimens and radiation damage

Richard D. Leapman *, Songquan Sun

Biomedical Engineering and Instrumentation Program, NCRR, Building 13, Room 3N17, National Institutes of Health, Bethesda, MD 20892, USA

Received 27 July 1994; in final form 14 November 1994

Abstract

Valence electron energy loss spectroscopy (EELS) has been used to characterize the composition of frozen-hydrated specimens in the electron microscope. Fine structure in the energy range up to 30 eV provides a means of distinguishing between vitreous and crystalline ice. Some features of the ice spectrum can be understood in terms of transitions between molecular orbitals in the water molecule and by the existence of excitons in the solid. Spectra from hydrated biological specimens can be analyzed to obtain quantitative estimates of the water content by fitting contributions from the ice and organic components. EELS also provides information about the radiation chemistry that occurs when hydrated specimens are exposed to the electron beam. From the observation of the hydrogen K-edge at ~ 13 eV, it can be deduced that bubbles of molecular hydrogen are evolved during irradiation at doses of $> 10^4$ nm^{-2}, and that these bubbles contain gas at pressures in excess of one thousand atmospheres.

1. Introduction

Cryo-electron microscopy is now an established technique for determining the structures of macromolecular assemblies that are preserved in their native aqueous state by vitrification [1,2]. It can also be used to determine subcellular structure [3] and water distributions [4,5] in tissue prepared by rapid freezing and cryosectioning. It is well known that the information obtainable from such specimens is limited by the quality of freezing and by their susceptibility to radiation damage in the electron beam [3]. In this paper we demonstrate how electron energy loss spectroscopy (EELS) provides a complementary tool to electron microscopy and diffraction for characterizing frozen-hydrated specimens and learning about their radiation chemistry. Cells typically contain about 80% water and 20% organic compounds, and each of these components is sensitive to radiation damage [3,6]. Together their radiation sensitivity is in fact enhanced by the reactions of free radicals (e.g., hydroxyl) with the organic molecules [7]. Clearly, EELS can be best applied to frozen-hydrated specimens by utilizing the valence excitations that can provide a reasonable signal at low electron dose. It is difficult to apply core excitations to these specimens because their relatively small scattering cross section results in too weak a signal. It is only recently that suitable instrumentation has become available to perform the cryo-EELS experiments. Require-

* Corresponding author.

SSDI 0304-3991(95)00019-4

ments for the instrumentation include: parallel-detection of the spectrum to minimize incident dose; cryotransfer specimen stage to avoid ice contamination and to maintain cryogenic temperatures; and preferably a cold field-emission source to provide a sub-1 eV energy resolution that is desirable for probing the chemical state. Few high resolution EELS measurements have previously been obtained from vitrified water or from vitrified aqueous solutions of organic compounds, although there do exist some earlier optical data on the different phases of ice [8]. It is therefore interesting to compare our results with the energy loss function obtained from these difficult optical measurements performed in the vacuum ultraviolet energy range. Our specific aims are to establish how the valence energy loss spectrum from vitrified water differs from that of hexagonal ice and to investigate some aspects of the radiation damage that occurs in hydrated organic specimens under conditions where the phenomenon of bubbling occurs. The nature of the gas inside these bubbles is of considerable interest and has been described as having strange properties [3]; until now its identity has not been known.

2. Experimental methods

Thin films of frozen vitreous water were prepared by pipetting drops of deionized water onto bare 600-mesh copper EM grids. The grids were then blotted with filter paper immediately prior to plunging into liquid ethane at −175°C, as first described by Adrian et al. [9], in our case by using a Leica KF80 freezing machine. Crystalline hexagonal ice was obtained by slowly immersing the blotted grids into liquid nitrogen. Both specimens were characterized by electron diffraction in a conventional transmission electron microscope (Hitachi H700H) to verify which phase was present [3].

Specimens of mouse liver that were rapidly frozen by a metal mirror cryofixation device (Delaware Diamond Knives, Inc.) were cryosectioned by means of a Reichert Ultracut E microtome equipped with an FC-4 cryo-attachment (Leica, Deerfield, IL) and an ionization device to reduce static charge build-up (Diatome-U.S., Fort Washington, PA) [10]. Cryosections were also obtained from frozen six-molar glycerol solution (containing approximately 50% water and about 6% bovine serum albumin); this solution which is commonly used as a cryopreservative could easily be vitrified even by slow cooling. The temperatures of the specimen, knife and microtome chamber were set to the lowest values of around −160°C for sectioning the liver and at somewhat higher values of around −130°C for the glycerol solution. The sections were manipulated with eyelash probes and placed on 200 hexagonal mesh copper grids coated with a thin ~ 20 nm Formvar/carbon support film.

Frozen specimens were cryotransferred at −180°C into a VG Microscopes HB501 scanning transmission electron microscope (STEM) (Fisons Instruments, San Carlos, CA) operating at a beam energy of 100 keV. The electron spectrometer was a Gatan parallel EELS (model 666) equipped with a 1024-channel photodiode array [11–13]. The field-emission source of the STEM provided incident electrons of 0.5 eV energy spread, defined by the full-width at half maximum of the zero-loss peak. Photodiode counts were converted into numbers of primary electrons by using the previously determined conversion factor of ~ 40 e/count. The energy dispersion was set to 0.1 eV/channel and a spectrometer acceptance semi-angle of ~ 10 mrad was chosen.

Electron energy loss spectra were acquired in two ways. First, specimens could be analyzed by means of the Gatan EL/P program running on an Apple Macintosh IIfx computer [14]. This provided a convenient means of recording spectra from the specimens of pure water and also from extended regions of the cryosection. An asynchronous spectrometer de-scan control (provided by the PC-486 computer) was employed to compensate for shift of the spectrum over the detector array at low magnifications. This was achieved by feeding a signal proportional to the specimen scan voltage to the drift tube of the spectrometer [15]. EELS data could thus be acquired at low dose (~ 10 e nm^{-2}) while maintaining an energy resolution of ~ 0.5 eV. To collect spectra from specific organelles in a cryosection the spectrum-

imaging approach was employed as described previously [16]. A PC-486 computer was used to collect spectra at each pixel in a 128×128 pixel array; spectra could then be summed over selected pixels to obtain information about specific subcellular compartments. No de-scan was needed to acquire the spectrum image data because the zero loss peak could be calibrated at each pixel. The realignment operation necessary to integrate spectra from extended areas of the specimen had the advantage of averaging out the channel-to-channel gain variations of the detector array [17]. The PC also acquired digital annular dark-field images that provided morphological information about the specimen [16].

The spectra were processed as follows: subtraction of the detector dark current, deconvolution of the detector point-spread function, and removal of plural inelastic scattering by the Fourier-logarithmic deconvolution method [18]. For the cryosectioned tissue a correction was also made to remove the inelastic scattering due to the support film [4]. The resulting spectrum could then be analyzed by fitting ice and protein reference spectra using a multiple least squares program.

3. Results and discussion

3.1. EELS of vitreous and crystalline ice

EELS provides a powerful means for investigating the electronic structure of solids over a wide energy range that is difficult to access by optical measurements in the vacuum ultraviolet. Although some earlier optical and EELS measurements on water exist [8,19,20] recent technical developments make it worthwhile to collect new data on this important substance. Ice is interesting because its molecules are held together solely by hydrogen bonds whose electronic structure is not well understood. Ice has three phases that can exist at low pressure in the electron microscope – hexagonal, cubic and vitreous [3].

Hexagonal ice is the commonly found structure that is easily obtained by slowly cooling the liquid. Specimens of hexagonal ice prepared for electron microscopy typically have crystal sizes in the micrometer range; an electron diffraction pattern from a typical single crystal is shown in Fig. 1a. Cubic ice has a very similar structure to that of the hexagonal phase and is formed by deposition of water vapor in a vacuum at temperatures of approximately -100°C to -130°C [3]. Crystals of the cubic structure are typically less than 100 nm in size, giving the ring diffraction pattern in Fig. 1b. Vitreous ice is formed at lower temperatures by deposition of water vapor in a vacuum or by rapidly cooling water at rates $> 10^5$ °C s^{-1}. The amorphous nature of this phase is evident in the diffuse rings of the electron diffraction pattern in Fig. 1c. At temperatures above -130°C vitreous ice undergoes a phase transition to the cubic structure. One might expect that vitreous ice would have a similar density to that of liquid water but experiments have shown that the density is $(0.93 \pm 0.02) \times 10^3$ kg m^{-3}, i.e., similar to that for hexagonal or cubic ice [3,21]. This low density implies that water expands by 2% or 3% during vitrification but electron diffraction measurements on vitrified protein crystals indicate that the change in lattice parameter is in fact $< 0.5\%$. Despite these unresolved questions about the density of vitreous ice it is clear that vitrification provides the best method for preserving biological structures in as close to their native state as possible.

Single scattering electron energy loss spectra from hexagonal, cubic and vitreous ice are presented in Fig. 2a. The spectrum from cubic ice is nearly identical to that from the hexagonal phase as expected because both structures have the same arrangement of four nearest neighboring water molecules around a central water molecule. A close similarity is also observed between the spectra from vitreous and crystalline ice. This correspondence in shape which was not evident in previous ultraviolet data [8] is clearly evident when the two spectra are superimposed (as shown in the top of Fig. 2a). A closer inspection, however, does reveal some significant differences in the features (a), (b) and (c) at energy losses of 10.8, 15.0 and 25.5 eV, respectively. In particular, the feature at ~ 15 eV shows up as a distinct

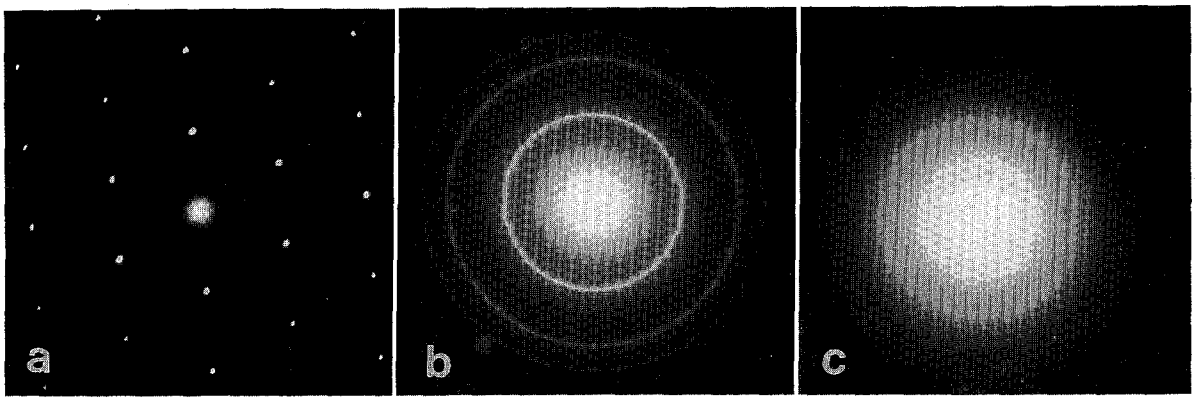

Fig. 1. Diffraction patterns of different phases of ice from which valence EELS spectra were recorded: (a) hexagonal, (b) cubic, (c) vitreous.

shoulder in crystalline ice but is much weaker in the vitreous structure (Fig. 2b). Similar observations have also been reported in the earlier optical measurements [8].

As described by Kobayashi [8] a crude assignment of some of the structure in the energy loss spectrum can be made by examining transitions from molecular orbital states of the water molecule and by making use of the optical absorption spectrum of water vapor obtained by Ishiguro et al. [22]. In the absorption spectrum from water vapor there is a broad band at 7.4 eV which is due to a transition from the $1b_1$ molecular orbital to a $4a_1$ molecular orbital, a second band at 9.7 eV due to a transition from the $3a_1$ to $4a_1$ orbitals, and a third band at around 13.7 eV due to transitions from the $1b_2$ to $4a_1$ orbitals. To match the energies of the first maxima we must displace the optical absorption spectrum to higher energies by ~ 1.5 eV; we then find that the features (a) and (b) coincide. This simple analysis would explain the origin of features (a) and (b) although it cannot predict the energies of the EELS plasmon maximum at 20.4 eV or the feature (c) at 25.5 eV. As discussed by Kobayashi [8] an excited electronic state in an insulating mate-

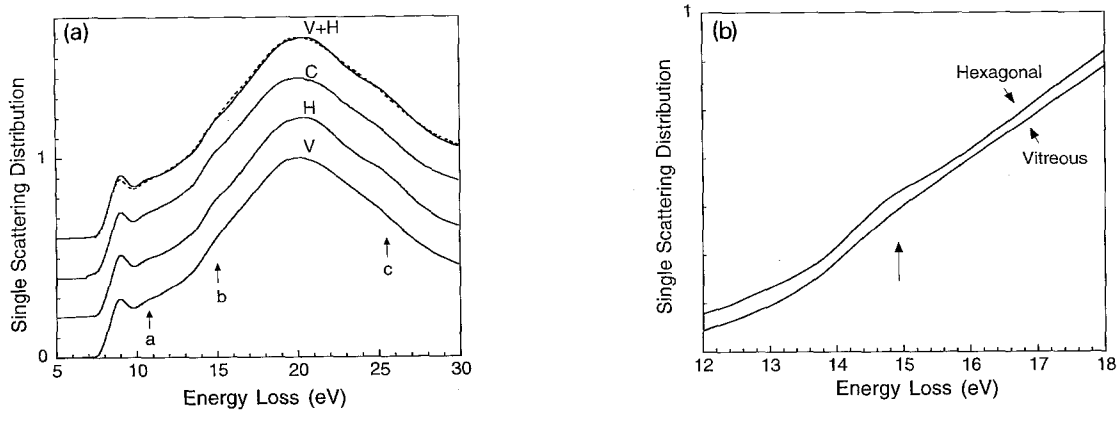

Fig. 2. (a) Single-scattering EELS from thin films of hexagonal ice (H), cubic ice (C) and vitreous ice (V) recorded at dose of < 100 e/nm^2; features (a), (b) and (c) are weaker in vitreous ice; spectra from vitreous ice (dashed line) and hexagonal ice (solid line) are superimposed above to show their similarity in shape. (b) Comparison of spectra from hexagonal and vitreous phases in energy range 12–18 eV showing stronger feature at 15 eV in crystalline ice.

rial must be described in terms of a localized exciton. The radii of highest electron density of the first three unoccupied Rydberg states of the water molecule are 0.2, 0.6 and 1.2 nm while the oxygen–oxygen distance between water molecules is 0.28 nm. These distances are a measure of the extension of the excited state in ice so the orbitals of higher excited states would extend over several neighboring molecules whereas the lowest state would be almost contained within one water molecule. If this interpretation is correct the first maximum at 9.1 eV in the EELS spectrum would correspond to the 1s exciton consisting of an electron in the $4a_1$ band and a hole in the $1b_1$ band; the second feature at 10.8 eV would correspond to the 2s exciton; and the exciton binding energy would be 2.3 eV. The fact that the feature at 10.8 eV is broader in vitreous ice than in crystalline ice might be explained by the radius of the second exciton extending into a disordered region of the structure.

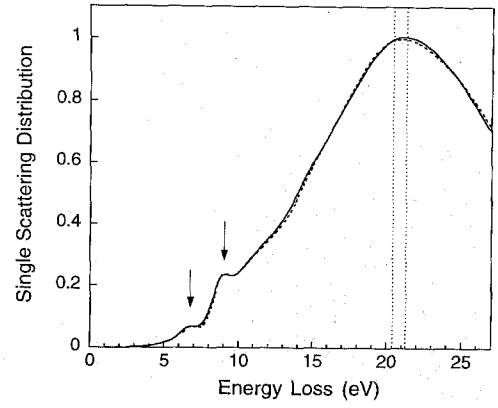

Fig. 3. Summed EELS from fifteen mitochondria in cryosection of rapidly frozen mouse liver (solid line) and multiple least squares fit to reference spectra from vitrified water and protein (dashed line); peak at 6.7 eV (arrow) is due to excitation of π-states in organic compounds, e.g., peptide bonds and aromatic groups in proteins; peak at 9.1 eV (arrow) is ice exciton; plasmon maximum at 21.3 eV is shifted up in energy by ~ 1 eV relative to ice spectrum.

3.2. EELS of frozen biological specimens

Compartments of cells typically contain $75 \pm 15\%$ water. For example, the cytoplasm has a water content of around 80% and the mitochondria 60% [23]. The compositions of most other organelles also fall in this range with a few exceptions like lipid droplets which do not contain any water and plant vacuoles which contain almost 100% water. The major organic constituents in cells are proteins, lipids, carbohydrates, and nucleic acids, with protein generally being the most abundant. Electron energy loss spectra from most of these compounds have a broad plasmon peak at ~ 23 eV as well as structure from 5 to 7 eV corresponding to excitation of π-states. A substantial difference in the EELS shape therefore exists between the organic compounds and ice (which has a plasmon at 20.4 eV, an exciton at 9.1 eV and no structure in the 5–7 eV range). Indeed, we have shown previously that the valence EELS from organelles in cryosectioned, rapidly frozen tissue can be modeled quite accurately by the sum of contributions from water and protein. By fitting water and protein reference spectra it is possible to obtain not only quantitative estimates for the water content but also to map these distributions at a spatial resolution of ~ 100 nm and a precision of $\pm 5\%$ as limited by counting statistics for the maximum allowed electron dose [5].

Fig. 3 is the summed spectrum from 15 mitochondria in a hydrated cryosection of mouse liver recorded at a dose of 2×10^3 e/nm^2 and at a temperature of -170°C; a multiple least squares fit to the water and protein reference spectra is also shown. In addition to the 9.1 eV water peak, there is a shoulder at 6.7 eV in the spectra from the mitochondria; this is mainly attributed to π-excitations of the peptide bonds in the protein. The plasmon maximum is also shifted up in energy by ~ 1 eV relative to pure ice as expected from the higher plasmon energy of the organic component. The ratio of fitting coefficients gave a water content of $56.8 \pm 2.0\%$ ($\pm$standard error of the mean) in good agreement with other measurements [23]. This determination required values for the ratio of cross section per unit mass for water to that for protein which we have previously estimated as 0.89 ± 0.03 [4].

It is possible to establish whether a frozen-hydrated specimen is properly vitrified by observing

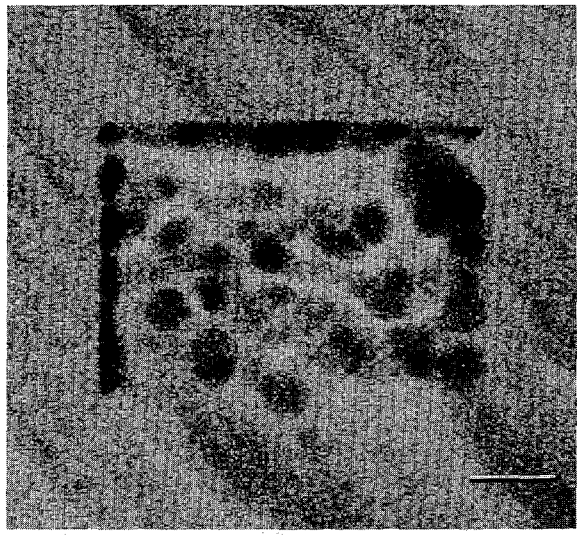

Fig. 4. Dark-field STEM showing bubble formation in 6-molar glycerol solution after exposure to dose of $\sim 5\times10^4$ e nm^{-2}. Bar = 100 nm.

the fine structure near 15 eV. As described above, a rounded shape at this energy indicates the vitreous state whereas a sharper shoulder indicates that crystallization has occurred. This observation is useful because it is often inconvenient to record the diffraction pattern at low electron dose in the STEM.

3.3. Radiation damage

Structural changes that occur when frozen-hydrated organic or biological specimens are irradiated in the electron microscope have been described in detail by several authors [3,24,25]. Here we show that EELS can be used to characterize beam damage effects and radiation chemistry in such specimens. Morphological observations show that above a dose of approximately 10^4 e/nm^2 numerous small bubbles appear which rapidly fuse together and continue to grow causing the specimen to deform. The bubbles eventually break when they extend to the surface of the specimen. As discussed by Dubochet et al. [3] bubbling appears in vitrified aqueous solutions of organic compounds and also in non-vitrified specimens between hexagonal ice crystals where the organic compounds are concentrated. Bubbling is not strongly dependent on dose rate and is reduced but still present even at near liquid helium temperatures of 4 K.

We have observed the bubbling effect both in cryosectioned liver and in cryosectioned 6-molar glycerol solution containing 6% bovine serum albumin; this solution is used for cryopreserving tissue. The liver has a water content of $\sim 75\%$ and the glycerol $\sim 50\%$, and the cryosections

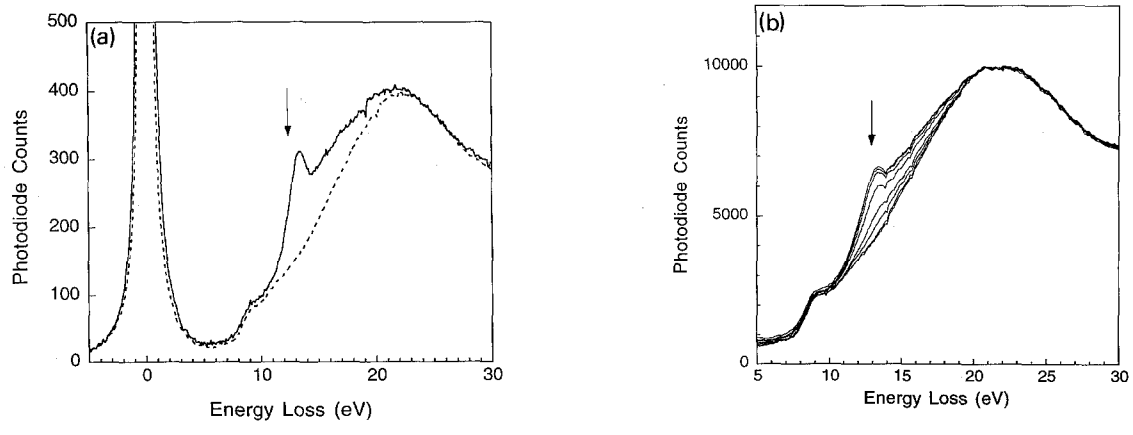

Fig. 5. (a) EELS recorded at temperature of -180°C from 200 nm thick cryosection of vitrified glycerol solution exposed to dose of 5×10^4 e nm^{-2} (solid line) and dose of $\sim 10^3$ e nm^{-2} (dashed line). (b) EELS from rapidly frozen mouse liver at eight incremental doses ranging from 5×10^3 e nm^{-2} to 4×10^4 e nm^{-2}. Peak at around 13 eV is attributed to hydrogen K-edge that forms concomitantly with bubbling of the specimen observed in dark-field STEM.

have a thickness of approximately one inelastic mean free path (~ 200 nm). Fig. 4 shows a dark-field STEM image from a glycerol specimen exposed to a dose of 5×10^4 e/nm^2; numerous bubbles are evident with typical diameters of 40 nm. Electron energy loss spectra were collected while the bubbling phenomenon was being observed in the STEM and these are shown in Fig. 5a and 5b for glycerol and liver, respectively. In both spectra sharp peaks appear at 13 eV with a threshold at around 12.3 eV. The peak continues to increase in strength as the bubbles become visible until their diameters reach approximately 50 to 100 nm when the peak is seen to disappear. Sometimes the peak reforms and disappears yet again as new bubbles are generated. Eventually a hole is etched in the specimen when the accumulated dose reaches $\sim 10^6$ e/nm^2. After scaling the intensities to match at 30 eV we can extract the shape of the 13 eV peak by subtracting the spectrum of the undamaged specimen from the spectrum recorded under conditions where bubbling occurred. No attempt was made to correct for plural inelastic scattering because the specimen thickness was not constant within the analyzed area during bubble formation. Despite the presence of some plural scattering the subtraction procedure now clearly reveals the presence of the hydrogen K-edge as shown in Fig. 6. The shape is seen to agree well with the spectrum from molecular hydrogen recorded by Ahn and Krivanek [26] and also with the earlier high resolution spectra of Geiger and Schmoranzer [27]. It is interesting however that we observe a slightly higher edge energy by approximately 0.5 eV. We conclude that the bubbles contain molecular hydrogen that is released due to free radical reactions occurring in the hydrated specimen. There is no evidence for the production of molecular oxygen which has a different characteristic spectrum with an L-edge at ~ 8 eV and a sharp pre-edge peak at ~ 5 eV [26]. The fact that bubbling is not observed in pure water, except at much higher doses and in thick specimens, indicates that the organic molecules play an essential role in the production of hydrogen; the water is not simply split into hydrogen and oxygen. If no organic molecules were present there would presumably be a high probability for recombination of the hydrogen and hydroxyl radicals. As discussed by Symons [7] the organic molecules could react rapidly with the hydroxyl radical to extract hydrogen. There are many possible reactions that could occur by ionization of atoms in the specimen and we cannot determine which of these are the most important. However, the following is one pair of reactions that would liberate molecular hydrogen:

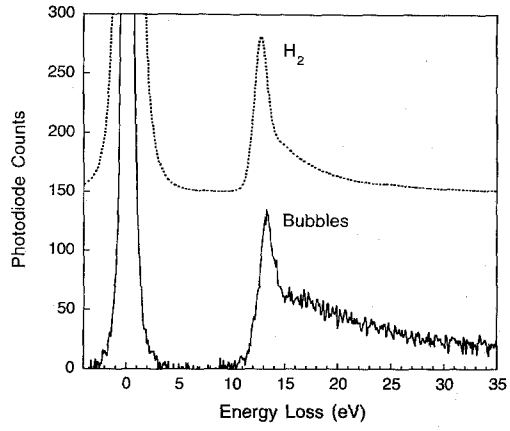

Fig. 6. Hydrogen K-edge from gas bubbles (solid line) obtained by subtracting the spectrum of undamaged glycerol from the spectrum of damaged glycerol – no correction was made for plural inelastic scattering. Comparison is made with spectrum from pure hydrogen gas (dashed line) recorded by Ahn and Krivanek [26].

$$H_2O \rightarrow H^{\cdot} + OH^{\cdot},$$

$$OH^{\cdot} + R\text{–}H \rightarrow RO^{\cdot} + H_2,$$

where R–H represents an organic molecule and one of its hydrogen atoms. It is interesting to estimate the pressure of the hydrogen bubbles embedded in the frozen-hydrated specimen. From the relative intensities of the hydrogen K-edge and the total low-loss signal, including zero-loss peak, we can determine the number of hydrogen molecules N_H per unit area of the damaged specimen [18]:

$$N_H \approx \tfrac{1}{2}[I_H(\Delta,\beta)/I_T(\Delta,\beta)][\sigma_H(\Delta,\beta)]^{-1},$$

where $I_H(\Delta,\beta)$ is the integrated signal in the hydrogen K-edge for energy range Δ and collection angle β, $I_T(\Delta,\beta)$ is the corresponding total

integrated signal in the low-loss spectrum, and $\sigma_H(\Delta, \beta)$ is the partial inelastic cross section for the hydrogen K-edge. The collection semi-angle β was 10 mrad and the integration range was 10 eV, which gives a calculated partial cross section per atom for the hydrogen K-edge of 1.75×10^{-23} m^2 $atom^{-1}$ for a beam energy of 100 keV. Notice that we include a factor of 1/2 in the above equation to provide the number of hydrogen molecules rather than the number of hydrogen atoms per unit area. This gives a value for the number of hydrogen molecules per unit area of the specimen as 2×10^{21} m^{-2}. From the known electron dose we therefore find that on average one hydrogen molecule is formed for roughly every 20 electrons incident on a specimen of thickness one inelastic mean free path. From images such as Fig. 4 we can also determine that there are about 300 hydrogen bubbles per square micrometer of the specimen and therefore approximately 7×10^6 hydrogen molecules per bubble. Since the bubbles have a mean diameter of ~ 50 nm, we can estimate the number of molecules per unit volume as $n_H = 10^{29}$ m^{-3} which is an extremely high density. If we assume that the hydrogen behaves as an ideal gas then:

$$P = n_H kT.$$

Putting in values for Boltzmann's constant k and the absolute temperature of $T \approx 100$ K, we obtain a pressure of $\sim 10^8$ N/m^2 which corresponds to ~ 1000 bars, and departure from ideal gas behavior makes this a lower estimate. It seems reasonable that small bubbles containing gas at even higher pressures would expand to reduce the stress in the solid. If the bulk elastic modulus were similar to that of hexagonal ice at -16°C which has a value of $\sim 10^{10}$ N m^{-2} [28] then the volume strain would be reduced to approximately 10^{-2}. Finally, we note that the high gas density in the bubbles may be responsible for the observed "blue-shift" upward in energy of the hydrogen K-edge by ~ 0.5 eV mentioned above. A similar phenomenon has been reported by Fink [29] for helium and this can be attributed to effects of the Pauli exclusion principle as the excited state wave function overlaps the ground state wave functions of surrounding atoms.

4. Conclusions

Cryo-electron energy loss spectroscopy of frozen-hydrated specimens provides useful information that is complementary to that obtained by cryo-electron microscopy. We have shown that the technique can distinguish between vitreous and crystalline ice and should therefore be helpful in characterizing hydrated specimens in the analytical electron microscope. At present we have a plausible explanation of some but not all the features in the ice spectrum in terms of molecular orbitals and excitons. The spectrum from frozen organic solutions and biological specimens can be quantified by considering a linear sum of contributions from the water and organic components, thus providing the basis for determining the subcellular water distribution in cryosectioned tissue. Finally, we have made an interesting observation regarding the radiation chemistry that occurs during the bubbling phenomenon in irradiated hydrated specimens. Molecular hydrogen was directly identified in the bubbles formed by free radical reactions and this may provide some further insight into the mechanisms of radiation damage at cryogenic temperatures [30,31].

Acknowledgements

The authors are indebted to Dr. S. Shi for assistance with the specimen preparation, to Dr. S.B. Andrews for helpful advice and discussions, and to Dr. J.A. Hunt for providing the EELS spectrum-imaging and de-scan systems.

References

[1] J. Dubochet, J.-J. Chang, R. Freeman, J. Lepault and A.W. McDowall, Ultramicroscopy 10 (1982) 55.
[2] J. Dubochet, J. Lepault, R. Freeman, J.A. Berriman and J.-Cl. Homo, J. Microscopy 128 (1982) 219.
[3] J. Dubochet, M. Adrian, J. Chang, J.-Cl. Homo, J. Lepault, A.W. McDowall and P. Schultz, Q. Rev. Biophys. 21 (1988) 129.
[4] S.Q. Sun, S.L. Shi and R.D. Leapman, Ultramicroscopy 50 (1993) 127.

[5] S.Q. Sun, S.L. Shi, J.A. Hunt and R.D. Leapman, J. Microscopy 177 (1995) 18.
[6] M.S. Isaacson, in: Principles and Techniques of Electron Microscopy VII, Ed. M.A. Hayat (Van Nostrand-Reinhold, New York, 1977) p. 1.
[7] M.C.R. Symons, Ultramicroscopy 10 (1982) 97.
[8] K. Kobayashi, J. Phys. Chem. 87 (1983) 4317.
[9] M. Adrian, J. Dubochet, J. Lepault and A.W. McDowall, Nature 308 (1984) 32.
[10] M. Michel, H. Gnägi and M. Müller, J. Microscopy 166 (1992) 43.
[11] O.L. Krivanek, C.C. Ahn and R.B. Keeney, Ultramicroscopy 22 (1987) 103.
[12] O.L. Krivanek, J.H. Paterson and H.R. Poppa, in: Proc. 47th Annual EMSA Meeting, Ed. G.W. Bailey (San Francisco Press, San Francisco, 1989) p. 410.
[13] R.D. Leapman and S.B. Andrews, J. Microscopy 161 (1991) 3.
[14] M. Kundmann, X. Chabert, K. Truong and O.L. Krivanek, EL/P Software for a Macintosh II Computer (Gatan Inc., 6678 Owens Drive, Pleasanton, CA 94566, USA, 1990).
[15] J.A. Hunt, R.D. Leapman and D.B. Williams, Microbeam Anal. 2 (1993) 272.
[16] J.A. Hunt and D.B. Williams, Ultramicroscopy 38 (1991) 47.
[17] H. Shuman and P. Kruit, Rev. Sci. Instr. 56 (1985) 231.
[18] R.F. Egerton, Electron Energy Loss Spectroscopy in the Electron Microscope (Plenum, New York, 1986) p. 229.
[19] J.A. LaVerne and A. Mozumder, J. Phys. Chem. 90 (1986) 3242.
[20] J. Daniels, Opt. Commun. 3 (1971) 240.
[21] O. Mishima, L.D. Calvert and E. Whalley, Nature 314 (1985) 76.
[22] E. Ishiguro, M. Sasamura, H. Masuko, Y. Morioka and M. Nakamura, J. Phys. B 11 (1978) 993.
[23] R.A. Buchanan, R.D. Leapman, M.F. O'Connell, T.S. Reese and S.B. Andrews, J. Struct. Biol. 110 (1993) 244.
[24] Y. Talmon, Ultramicroscopy 14 (1984) 305.
[25] R.M. Glaeser and K.A. Taylor, J. Microscopy 112 (1978) 127.
[26] C.C. Ahn and O.L. Krivanek, EELS Atlas (Arizona State University Center for Solid State Sciences, Tempe, AZ and Gatan Inc., Warrendale, PA, 1983).
[27] J. Geiger and H. Schmoranzer, J. Mol. Spectrosc. 32 (1969) 39.
[28] D.E. Gray, Ed., American Institute of Physics Handbook, 3rd ed. (McGraw Hill, New York, 1972) p. 2–53.
[29] J. Fink, Adv. Electron. Electron Phys. 75 (1989) 121.
[30] A. Henglein, Ultramicroscopy 14 (1984) 195.
[31] Use of brand names does not constitute or imply endorsement.